RSC Advances

PAPER

View Article Online
View Journal | View Issue

Cite this: *RSC Adv.*, 2018, **8**, 8569

Effects of oxygen functional groups and $FeCl_3$ on the evolution of physico-chemical structure in activated carbon obtained from Jixi bituminous coal†

Dongdong Liu,[ad] Boyin Jia,*[b] Xiujuan Liu,[c] Bojun Zhao,[d] Jihui Gao,*[d] Qingxi Cao,[d] Shaohua Wu[d] and Yukun Qin[d]

It is crucial to increase the values of S_{BET}/burn-off ratio to achieve activated carbon (AC) with a higher SO_2 adsorption capacity at a low cost from flue gas. In this study, at first, Jixi bituminous coal was used as a raw material to prepare a series of pre-treated samples by oxidation treatment and adding different amounts of the $FeCl_3$ catalyst. Then, the AC samples were prepared by pyrolysis under a N_2 atmosphere and physical activation with CO_2. Finally, the change in the physico-chemical structure of different samples was determined to study the effects of oxygen functional groups and $FeCl_3$. The results show that the rapid growth of mesopores is mainly influenced by the evolution of oxygen functional groups, whereas the micropores are mainly influenced by the $FeCl_3$ catalyst during pyrolysis. These effects can also further improve the size and the carbon type of the aromatic structure from a different perspective to promote the disordered microstructure of treated chars (1FeJXO15-800H, 3FeJXO15-800H and 6FeJXO15-800H) as compared to the ordered microstructure and less pores of the un-pretreated char (JX-800). Then, the active sites can no longer be consumed preferentially in the presence of the catalyst; this results in the continuous disordered conversion of the microstructure as compared to the ordered conversion of JX-800 char during activation. On the one hand, the developed initial pores of 1FeJXO15-800H, 3FeJXO15-800H, and 6FeJXO15-800H chars promote the favorable diffusion of activated gas, following the non-hierarchical development. On the other hand, the presence of Fe-based catalysts facilitates the etching of carbon structure and the rapid and continuous development of the micropores, hindering the severe carbon losses on the particle surface. Finally, the 3FeJXO15-800H char with a high value of S_{BET} (1274.64 $m^2\ g^{-1}$) at a low burn-off value (22.5%) has the highest S_{BET}/burn-off ratio value of 56.65 $m^2\ g^{-1}$/%, whereas the JX-800 char with a low value of S_{BET} (564.19 $m^2\ g^{-1}$) at a burn-off value of 58.2% has the lowest S_{BET}/burn-off ratio value of 9.69 $m^2\ g^{-1}$/%. Therefore, the presence of oxygen functional groups and $FeCl_3$ has obviously changed the evolution of the physico-chemical structure in activated carbon to effectively enhance the values of S_{BET}/burn-off.

Received 30th November 2017
Accepted 12th February 2018

DOI: 10.1039/c7ra12928a

rsc.li/rsc-advances

1 Introduction

At present, biomass is mainly used as a raw material for the preparation of activated carbon (AC). Because of the limited sources of raw materials, the production of biomass-based AC is relatively low and its price is relatively high. However, anthropogenic SO_2 emission from large coal-fired power plants has been considered as a major gas pollutant for a long time. Traditional biomass-based AC is unable to satisfy the desulfurization requirements in coal-fired power plants; therefore, AC can be produced by coal as the most suitable raw material instead of traditional biomasses and some wastes and the traditional physical activation with steam or CO_2 resulting from high-temperature flue gas. A higher specific surface area (S_{BET}) is conducive for desulfurization in the existence of a hierarchical structure (micro- and mesopores).[1–4] At present, industrial application of coal-based AC has been hindered owing to the relatively low desulfurization property and the relatively high cost, and these are associated with more carbon loss on the particle surface that cannot promote the number of pores during activation; this results in lower values of the S_{BET}/burn-

[a]College of Engineering and Technology, Jilin Agricultural University, Changchun 130118, China
[b]College of Animal Science and Technology, Jilin Agricultural University, Changchun 130118, China. E-mail: jiaboyin@139.com
[c]Petrochina Daqing Petrochemical Company, Daqing 163000, China
[d]School of Energy Science and Engineering, Harbin Institute of Technology, Harbin 150001, China. E-mail: gaojihui0809@163.com

† Electronic supplementary information (ESI) available. See DOI: 10.1039/c7ra12928a

off ratio. In previous years, coal-based AC with the S_{BET} values between 500 and 800 $m^2\ g^{-1}$ at the high burn-off values of approximately around 40–60% during activation has been produced by most of the researchers using physical activation.[5–7] Substantially, higher values (200–1100 $m^2\ g^{-1}$) have been reported by San Miguel *et al.*[8] for activation with steam and CO_2 at 925–1100 °C, but with burn-off levels up to 80%. These results show that it is necessary to operate at high burn-off to reach a higher S_{BET} *via* physical activation. However, it is difficult to obtain coal-based AC with a higher S_{BET} at low burn-offs during activation only by adjusting the activation conditions (such as temperature and type and dosage of the activating gases).[9,10] The specific analysis is as follows: the number of initial pores of precursors produced by pyrolysis and the conversion tendency of the carbon structure of precursors during activation have important effects on the ideal AC production. At first, in the beginning of the activation process, a small amount of initial pores can hinder the diffusion of the activated gas into the particles' interior to produce more pores; this leads to the occurrence of more reactions on the particle surfaces.[11–14] Then, with an increase in the activation time, the highly ordered conversion of the carbon structure at high temperatures can reduce the number of active sites; this hinders the sustained growth of micropores inside the particles and continually increases the external loss of quality.[15] Therefore, the simultaneous resolution of the abovementioned two problems is the key to achieve a high S_{BET}/burn-off value.

Most of the studies reported in literature suggest that the simultaneous introduction of oxygen functional groups produced by air pre-oxidation and metal catalysts may solve the abovementioned problems. At first, more pores in precursors can be produced by the evolution of oxygen functional groups during pyrolysis.[5,6,16] Francisco *et al.*[17–21] showed that the evolution of oxygen functional groups changed the pore development, and the mesopores were first produced followed by the formation of micropores with an increase in the cyclic oxygen chemisorption–desorption number. In a former study,[22] we reported that more active sites and a porous structure of oxidized chars were created by the evolution of oxygen-containing structures with different stabilities; this led to the rapid diffusion of the activated gas into the particles' interior during activation. However, the rapid consumption of oxygen-containing active sites and ordered conversion of carbon structure occurred with an increase in the activation time; this led to high burn-off. Then, the existence of metal catalysts may improve the conversion of the carbon structure that promotes gasification efficiency. The catalytic mechanism of gasification has been investigated by some researchers.[23–26] They believed that some intermediates (such as C(O) and M–C–O) were formed first in the presence of catalysts, and then, these intermediates acted as active sites that could react with a gasifying agent to increase the gasification rate. In addition, in our previous study,[27] we found that $FeCl_3$ at different amounts could improve the decomposition and condensation of the microstructures during pyrolysis in various degrees. However, the rapid polymerization of Fe-based catalysis led to severe deactivation of catalysts, and there were not enough initial pores in the Fe-based precursor to ensure gas diffusion during activation; this led to a relatively low S_{BET}/burn-off ratio value, which was in a good agreement with other studies.[28,29] Therefore, the effects of each oxygen functional group and $FeCl_3$ catalysts have been independently analyzed in our previous study. However, the effects of oxygen functional groups and Fe-based catalyst on the evolution of the physico-chemical structure in the process of formation of AC have rarely been studied in detail.

In this study, a series of coal samples were prepared by pre-oxidation in air at 200 °C for 15 h and loading various amounts of the $FeCl_3$ catalyst (1 wt%, 3 wt%, and 6 wt%) as a cheap metal catalyst into the coal. The effects of oxygen functional groups and $FeCl_3$ catalyst on the physical and chemical structure of coal char in the whole preparation process were investigated. The feature parameters of all the samples were obtained by transmission electron microscopy (TEM), scanning electron microscopy (SEM), nitrogen adsorption, X-ray diffraction (XRD), and Raman spectroscopy.

2 Experimental

2.1. Sample preparation

Jixi bituminous coal from China was used in this experiment, which was crushed and sieved to a particle size of 250–380 μm. To eliminate the interference of ash in coal, the sample coal was processed using 6 mol L^{-1} HCl and 40 wt% HF sequentially in accordance with the demineralization procedure.[30] After the demineralization procedure, the proximate and ultimate analysis data of the acid-treated samples were obtained, as shown in Table 1. The ash content in the acid-treated sample was below 1%, and this sample was denoted as JX. Then, JX was oxidized in air at 200 °C for 15 h and was denoted as JXO15; moreover, a predetermined amount of $FeCl_3$ powder (0.03 g, 0.09 g, and 0.18 g) and 3 g of oxidized coal (JXO15) were added to an aqueous solution. The resulting mixture was stirred for 24 h in a sealed beaker at ambient temperature, evaporated under vacuum, and dried at 100 °C overnight before the pyrolysis experiment; these samples were denoted as 1FeJXO15, 3FeJXO15, and 6FeJXO15.

2.2. Experimental process

The activated carbon was prepared by a conventional fixed bed reactor, and the more detailed process is as follows: (1) pyrolysis experiment: 3 g of the sample coals (JX, 1FeJXO15, 3FeJXO15, and 6FeJXO15) were placed in a three-stage fixed-bed reactor that was then heated at 8 °C min^{-1} to 800 °C and then

Table 1 Proximate and ultimate analyses of the acid-treated sample

	Proximate analysis (wt%)				Ultimate analysis (wt_{daf}%)				
Sample	V_{ad}	FC_{ad}	A_{ad}	M_{ad}	C_{daf}	H_{daf}	O_{daf}[a]	N_{daf}	S_{daf}
JX	39.66	56.60	0.12	3.62	74.81	19.49	4.01	1.31	0.38

[a] By difference; ad (air-dried basis): the coal in dry air was used as a benchmark; daf (dry ash free basis): the remaining component after the removal of water and ash in coal was used as a benchmark.

maintained for 60 min in a N_2 flow of 450 mL min^{-1}. Next, the sample coals were rapidly cooled under a N_2 atmosphere and denoted as JX-800, 1FeJXO15-800, 3FeJXO15-800, and 6FeJXO15-800. To eliminate the interference of Fe-based compounds in chars for the results of XRD and Raman, some char samples including Fe-based compounds were treated with 0.2 mol L^{-1} HCl and washed with distilled water to remove chloride ions; these samples were denoted as 1FeJXO15-800H, 3FeJXO15-800H, and 6FeJXO15-800H. Fig. S1† shows the XRD phase analysis results of 6FeJXO15-800 and 6FeJXO15-800H. (2) Activation experiment: these typical chars were continuously heated up to 900 °C under a N_2 atmosphere and then held for appropriate times under a CO_2 flow of 450 mL min^{-1} to obtain AC with different porous structures at different burn-offs. After activation, the CO_2 flow was replaced with N_2 to cool them down to room temperature. In addition, the char samples still included Fe-based compounds, which could interfere with the measurements and curve-fitted results of XRD and Raman owing to their fluorescence effects.[31,32] In order to obtain accurate results, some AC samples including Fe-based compounds was treated using 0.2 mol L^{-1} HCl, and these treated samples were denoted as JX-800, 1FeJXO15-800H, 3FeJXO15-800H, and 6FeJXO15-800H-burn-off values.

2.3. Measurement analysis

The transmission electron microscope (TEM, Tecnai G2 F30) was operated at 200 kV to visualize the structural changes. SEM (Quanta 200) was performed using an instrument operated at 200 kV to visualize the surface topography of samples. Structural parameters of the crystalline structures were obtained by the D/max-RB X-ray diffractometer, with the measurements performed in the 2θ range from 10° to 80° at a scan rate of 3° min^{-1}. Next, the char powders were investigated by Raman spectroscopy using a 532 nm wavelength laser and observing the scattering in the range of 1000–1800 cm^{-1}. The pore structure characteristics of the prepared samples were obtained by nitrogen adsorption at the analysis temperature of 77 K using a Micromeritics adsorption apparatus (ASAP2020), with the measurements performed for the adsorption data in the relative pressure (P/P_0) range from 10^{-7} to 1.[33] The prepared samples were degassed under vacuum at 473 K for 12 h before N_2 adsorption analysis. The specific surface area (S_{BET}), the micropore area (S_{mic}), the micropore volume (V_{mic}), and pore size distribution were calculated using the Brunauer–Emmett–Teller (BET) equation, *t*-plot method, Horvath-Kawazoe (HK) method, and the nonlocal density functional theory (NLDFT), respectively.[34–36] In addition, the total pore volume (V_t) was determined at the 0.98 relative pressure.

3 Results & discussion

3.1. TEM analysis of coal chars produced by pyrolysis

Several TEM images of different coal chars at a high resolution are shown in Fig. 1. A large amount of ordered crystalline layers could be found near a small quantity of amorphous carbon for JX-800, as shown in Fig. 1(a). Then, as the amount of $FeCl_3$ additive increased from 1 wt% to 3 wt%, there were more interlaced arrangements between amorphous carbon and crystallite layers and a lot of amorphous regions for 1FeJXO15-800 and 3FeJXO15-800, as shown in Fig. 1(b) and (c), indicating that the degree of order in microstructure decreased obviously. However, sphere-like particles encapsulated by multi-layer amorphous carbons can be found near some long, parallel-aligned crystallite layers having different orientations for 6FeJXO15-800, as shown in Fig. 1(d), and this phenomenon is related to the mechanism of metal-catalyzed graphitization.[37–39] Compared to the literature[27] regarding the TEM image (unoxidized coal chars with 6 wt% $FeCl_3$), closely arranged crystalline layers of 6FeJXO15-800 were broken, and blurred boundaries of crystalline layers, smaller diameter, and more amorphous regions were also observed in Fig. 1(d). The abovementioned results show that the existence of oxygen functional groups can hinder the concentration and amalgamation of the $FeCl_3$ catalyst at high temperatures; thus, the effects of oxygen functional groups and $FeCl_3$ catalyst can promote the obvious disordered arrangement of the microstructure during pyrolysis.

3.2. Pore structure analysis of coal chars produced by pyrolysis

The N_2 adsorption isotherms and the pore-size distribution of different coal chars are shown in Fig. 2. At first, the N_2 adsorption capacities of JX-800 were very small, indicating fewer pores. This result is related to the formation of metaplast materials that block the pores during pyrolysis. Then, the N_2 adsorption isotherms of 1FeJXO15-800H, 3FeJXO15-800H, and 6FeJXO15-800H were related to a type I at low pressures and type IV at high pressures according to the IUPAC classification. These isotherms began to branch, and a hysteresis loop could be observed as the relative pressure continued to increase; this indicated the formation of mesopores. With an increase in the amount of $FeCl_3$ additive from 1 wt% to 3 wt%, the N_2 adsorption capacities at low pressures increased evidently and their knee became broader; however, 6FeJXO15-800H exhibited an obvious decrease at low pressures; then, there were no obvious changes in their isotherms at high pressures. Alternatively, the pore-size distributions of different coal chars were relatively broad, where the size range was 0.6–20 nm, as observed from Fig. 2(b). As the amount of $FeCl_3$ addition increased from 1 wt% to 3 wt%, the volume of the micropores obviously increased; this indicated an increase in the micropore quantity and the presence of wider micropores. These changes might be related to catalytic cracking characteristics of $FeCl_3$. Gong *et al.*[30] proved that the cleavage of the microcrystalline structure was occurred by adding Fe-based catalysts to release more volatile matter (such as CO or CO_2); this led to formation of pores. However, the micropore volume in 6FeJXO15-800H exhibited an obvious decrease, which was related to the concentration and amalgamation of $FeCl_3$ catalyst at high temperatures. In addition, the size distribution of their mesopores was similar, but an increase in mesopore volume from 3 to 5 nm for 6FeJXO15-800H was observed by removing the nanoparticles occupying the inner space of coal chars. These

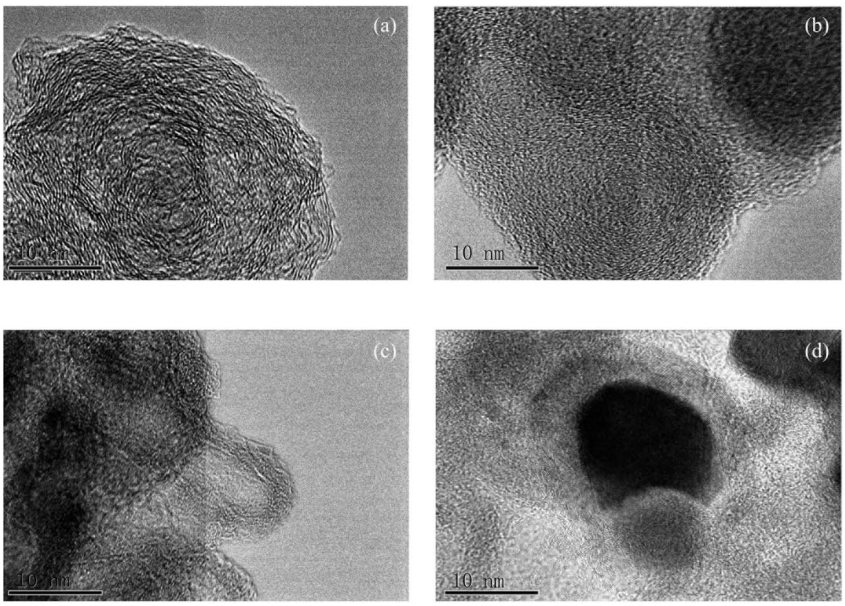

Fig. 1 TEM images of coal chars with different amounts of $FeCl_3$ (a) JX-800; (b) 1FeJXO15-800; (c) 3FeJXO15-800; and (d) 6FeJXO15-800.

results indicated that the evolution of oxygen functional groups mainly facilitated the development of mesopores, and the $FeCl_3$ catalyst could efficaciously promote the formation of micropores during pyrolysis. Therefore, the effects of oxygen functional groups and $FeCl_3$ catalyst can simultaneously promote the development of mesopores and micropores of coal chars during pyrolysis.

3.3. Crystal structure analysis of coal chars produced by pyrolysis

The XRD profiles of different coal chars are given in Fig. 3. There were two obvious broad diffraction peaks at $2\theta = 24°$–$27°$ and $41°$–$44°$ in all the samples, which were related to an interplanar spacing between two aromatic layers and the degree of condensation of aromatic layers.[40] According to the peak fitting treatment used by Liu *et al.*,[27] the XRD profiles of all the samples were processed to obtain some important parameters (such as the aromatic structure layer distance d_{002}, stacking height L_c, width L_a, and the number of aromatic layers $N = L_c/d_{002}$) regarding the microcrystalline structure, as shown in Table 2.

The 002 and 100 peaks observed for JX-800 were most obvious, the d_{002} value reached a minimum of 3.50 Å, and the L_c value reached a maximum of 13.72 Å as compared to that of other samples. The microcrystalline structure of JX-800 was transformed into a highly ordered graphite-like structure because of the presence of a plastic behavior. The appearance of the metaplast material facilitated the movement and orientation adjustment of aromatic layers during pyrolysis; this resulted in the rapid stacking and condensation of aromatic layers.[5,6,11–14] Then, the L_a, L_c, and N values of 1FeJXO15-800H, 3FeJXO15-800H, and 6FeJXO15-800H decreased, and the d_{002} values increased; this indicated that the microcrystalline structure was transformed into a type of

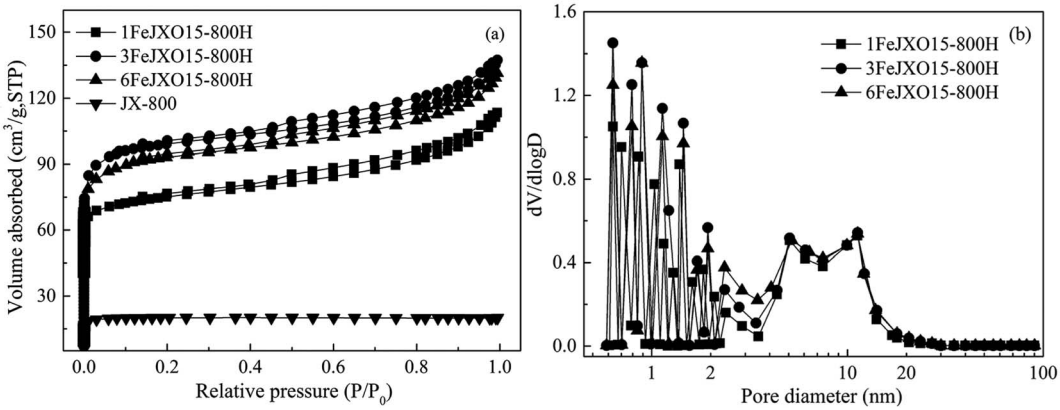

Fig. 2 N_2 adsorption isotherms and pore-size distributions of different coal chars obtained at 800 °C.

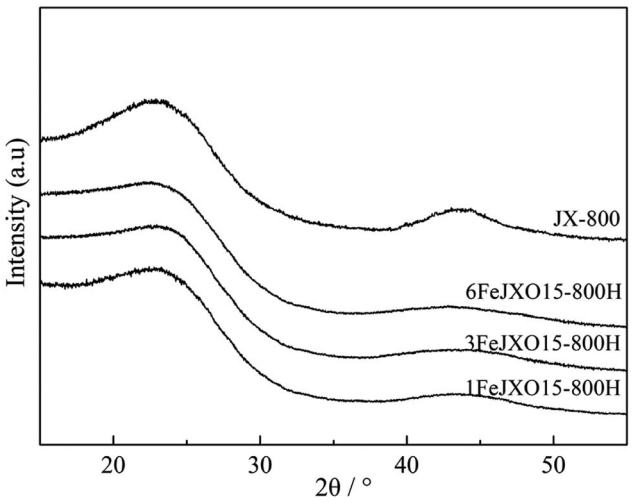

Fig. 3 XRD profiles of different coal chars obtained at 800 °C.

Table 2 XRD data of different coal chars obtained at 800 °C

	JX-800	1FeJXO15-800H	3FeJXO15-800H	6FeJXO15-800H
L_a (Å)	24.91	25.71	25.55	25.13
L_c (Å)	13.72	12.95	12.86	12.43
d_{002} (Å)	3.50	3.69	3.72	3.76
N	3.77	3.51	3.50	3.31

disordered structure during pyrolysis in the presence of $FeCl_3$ catalyst and oxygen functional groups. Compared to that of the oxidized char (JXO15-800) without the addition of the $FeCl_3$ catalyst reported in our previous study,[22] the degree of disorder in 1FeJXO15-800H, 3FeJXO15-800H, and 6FeJXO15-800H was further promoted by increasing the amount of $FeCl_3$ catalyst, and Fe might penetrate into an aromatic structure during pyrolysis to enlarge the aromatic structure layer distance (d_{002}). Alternatively, the decrease in the L_a and L_c values was related to the catalytic cracking characteristics of the $FeCl_3$ catalyst during pyrolysis. Murakami and William *et al.*[41,42] found that Fe-based compounds promoted the decomposition of aromatic structure to form more free radicals at the beginning of pyrolysis and then also hindered the further polymerization of free radicals to form a disordered microstructure at a later stage of pyrolysis. The above-mentioned results indicated that the effects of oxygen functional groups and $FeCl_3$ catalyst can further simultaneously improve the size of the microcrystalline structure from a different perspective to promote the degree of disorder in aromatic structure during pyrolysis; however, the catalytic cracking characteristics of the $FeCl_3$ catalyst might play a more important role in hindering the vertical stacking and condensation of aromatic layers during pyrolysis.

3.4. Carbon structure analysis of coal chars produced by pyrolysis

The Raman spectra of the different coal chars are shown in Fig. 4. The assignment of the five bands was carried out according to the peak fitting treatment using five bands reported by Li *et al.*[43] The Raman spectra of all the samples were processed with a smoothing function, baseline correction, and normalization using the Origin 9.1 software to obtain the parameters of different hybrid carbon structures. Importantly, the different band area ratios represent relative structure,[44,45] and this is ascribed to the following: (1) A_{D1}/A_G can be related to defect degree of the microcrystalline structure; (2) A_{D3}/A_G is considered as amorphous carbon; (3) A_{D1}/A_{D3} can indicate the ratio between big rings relative to small fused rings in chars; and (4) A_{D4}/A_G can be described as the relative quantity of cross-

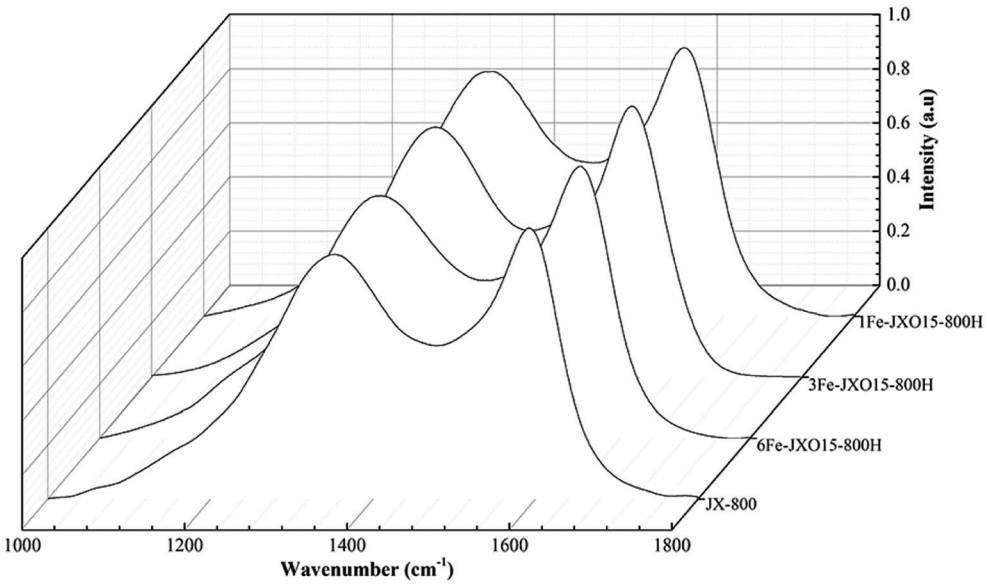

Fig. 4 Raman spectra of different coal chars obtained at 800 °C.

Table 3 Raman data of different coal chars obtained at 800 °C

	JX-800	1FeJXO15-800H	3FeJXO15-800H	6FeJXO15-800H
A_{D1}/A_G	3.197	3.770	3.877	3.987
A_{D3}/A_G	1.922	2.715	2.820	2.955
A_{D4}/A_G	0.611	0.849	0.885	0.936
A_{D1}/A_{D3}	1.663	1.388	1.375	1.349

linking bonds. In particular, the defect (A_{D1}/A_G) and cross-linking bonds (A_{D4}/A_G) can also be related to active sites in the samples. The parameters of carbon structure of carbonized chars are given in Table 3.

The narrow full width at half maximum of the D peak and G peak were observed for JX-800, as shown in Fig. 4. The A_{D1}/A_G, A_{D3}/A_G, and A_{D4}/A_G values of JX-800 reached minima, whereas the A_{D1}/A_{D3} value of JX-800 reached a maximum as compared to that of other samples; this indicated the presence of an ordered material with lower reactivity. Then, the A_{D1}/A_G, A_{D3}/A_G, and A_{D4}/A_G values of 1FeJXO15-800H, 3FeJXO15-800H, and 6FeJXO15-800H increased, whereas the A_{D1}/A_{D3} values decreased. These changes in hybrid carbon structures led to an increase in reactivity during pyrolysis. Compared to the oxidized char (JXO15-800) without the addition of $FeCl_3$ catalyst reported in our previous study,[22] the degree of change in 1FeJXO15-800H, 3FeJXO15-800H, and 6FeJXO15-800H was promoted further by increasing the amount of $FeCl_3$ catalyst; this presented more disordered conversion of the carbon structure during pyrolysis. These results indicated that Fe-based components hindered the transformation of the isolated and defective sp^2 structure (D_1 peak) into the crystalline sp^2 structure (G peak) and promoted the splitting of big aromatic rings (D_1 peak) to form the amorphous sp^2 bonding carbon atoms (D_3 peak); this led to a decrease in A_{D1}/A_{D3}. In addition, the metal components (M) might link with the carbon matrix and oxygen functional groups to form a C–O–M bond during pyrolysis; this would result in an increase in the sp^2–sp^3 bonding carbon atoms (D_4 peak).[41] These results indicate that the effects of oxygen functional groups and $FeCl_3$ catalyst can further improve the conversion of the carbon structure during pyrolysis to promote the number of active sites including the defects, the cross-linking bonds, and small aromatic rings, and the existence of oxygen functional groups can further promote the catalytic characteristics of the $FeCl_3$ catalyst during pyrolysis.

3.5. Crystal structure analysis of typical chars during activation

The XRD profiles and parameters of JX-800, 1FeJXO15-800H, 3FeJXO15-800H, and 6FeJXO15-800H at different burn offs during activation are shown in Fig. 5 and Table 4.

There was a sustained increase in the L_a value and decrease in the d_{002} value for JX-800, and the L_c value first decreased at low burn offs from 0 to 15.4% and then increased from 15.4 to 58.2%, as shown in Table 4. It can be concluded that the microcrystalline structure has transformed into a highly ordered structure during activation. At the beginning of activation, the defects and some sandwich materials (such as aliphatic side chain and amorphous carbon) of the longitudinal aromatic layer were removed gradually; this resulted in a decrease in the d_{002} and L_c values. With an increase in carbon loss, the longitudinal aromatic layers began to condense and distort; this increased the thickness of the microcrystalline structure. The sustained increase of the L_a value was related to the rapid condensation of transverse aromatic layers because of the ordered orientation of aromatic layers produced by pyrolysis.

Alternatively, there was a sustained increase in the d_{002} value and a persistent decrease in the L_a and L_c values for 1FeJXO15-800H, 3FeJXO15-800H, and 6FeJXO15-800H with an increase in burn offs. At the beginning of activation, oxygen-containing active sites were removed gradually by active gas; thus, the addition of $FeCl_3$ catalyst had promoted the disordered conversion of the microcrystalline structure during activation. In the catalytic process, the longitudinal aromatic structure condensed and distorted, and this occurred simultaneously with catalytic cracking; this resulted in an obvious decrease in the L_c value. Iron atom might have been bonded and fixed to carbon matrix, which destroyed the parallelism of the layer and

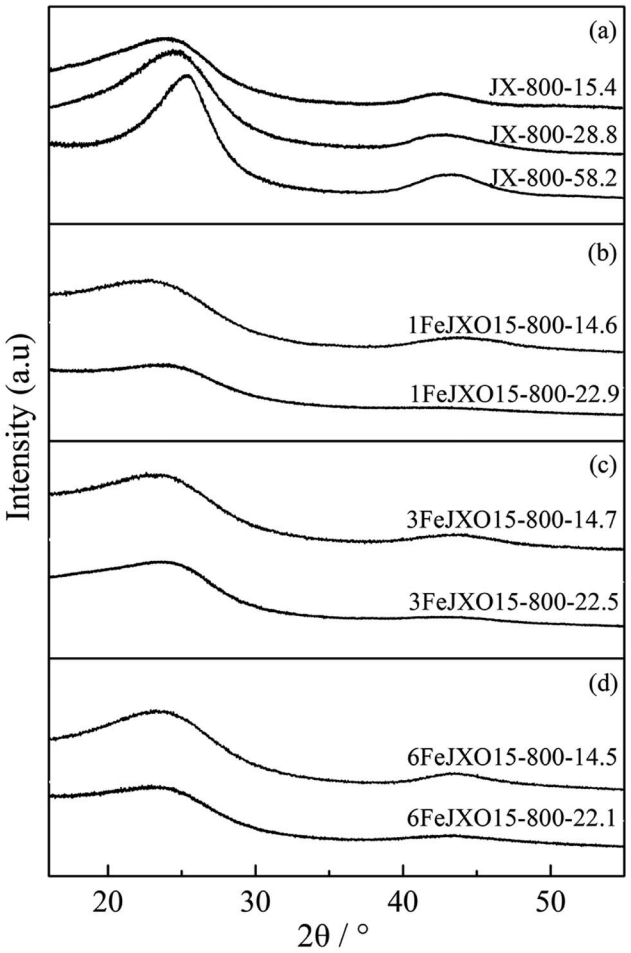

Fig. 5 XRD profiles of coal chars at different burn offs during activation.

Table 4 XRD data of coal chars at different burn offs during activation

Samples	L_a (Å)	L_c (Å)	d_{002} (Å)	N
JX-800	24.91	13.72	3.50	3.77
JX-800-15.4	25.37	13.41	3.45	3.89
JX-800-28.8	26.78	13.92	3.36	4.14
JX-800-58.2	28.35	15.53	3.11	4.99
1FeJXO15-800H	25.71	12.95	3.69	3.51
1FeJXO15-800H-14.6	25.12	12.35	3.80	3.25
1FeJXO15-800H-22.9	22.67	10.91	4.32	2.53
3FeJXO15-800H	25.55	12.86	3.72	3.50
3FeJXO15-800H-14.7	24.88	12.19	3.90	3.13
3FeJXO15-800H-22.5	22.21	10.42	4.55	2.29
6FeJXO15-800H	25.13	12.43	3.76	3.31
6FeJXO15-800H-14.5	24.91	12.21	3.84	3.18
6FeJXO15-800H-22.1	23.76	11.20	4.16	2.69

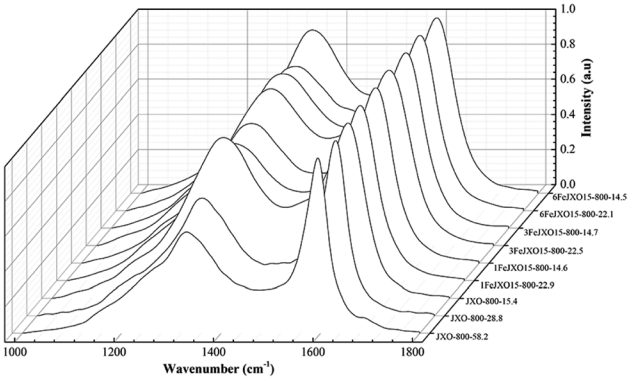

Fig. 6 Raman spectra of coal chars at different burn offs during activation.

the constancy of the interlayer spacing, thus increasing the interlayer spacing (d_{002}). Fe-based compounds accelerate the etching of crystallite and always hinder the condensation and growth of crystallite simultaneously. However, the changed degree of XRD parameter for 6FeJXO15-800H decreased gradually at the high burn-off values ranging from 14.5 to 23.76%. The aggregation of the $FeCl_3$ catalyst inside chars at high activation temperatures weakens the catalytic capacity, strengthening the condensation of longitudinal and transverse aromatic layers.

3.6. Carbon structure analysis of typical chars during activation

The Raman spectra and carbon structure parameters of JX-800, 1FeJXO15-800H, 3FeJXO15-800H, and 6FeJXO15-800H at different burn offs during activation are shown in Fig. 6 and Table 5.

There was a sustained decrease in the A_{D3}/A_G and A_{D4}/A_G values, whereas A_{D1}/A_{D3} and A_{D1}/A_G values first increased at the low burn offs ranging from 0 to 28.8% and then decreased from 28.8 to 58.2% for JX-800. At the beginning of activation, the smaller aromatic ring structure and active sites (such as cross-linking bonds) were consumed by activated gas preferentially. On the one hand, aromatic ring grew due to the dehydrogenation of hydro-aromatics during activation;[44] on the other hand, the small aromatic ring structures might react with activated gas or convert into big aromatic ring structures at high activation temperatures;[46] this resulted in a decrease in the A_{D3}/A_G and A_{D4}/A_G values and increase in the A_{D1}/A_{D3} and A_{D1}/A_G values. At the high burn-off from 28.8 to 58.2%, while the smaller aromatic ring structures were removed or changed preferentially, the inner aromatic structure could be activated by the continuous penetration of the activated gas; this could further induce the condensation of the aromatic ring and promote the formation of the crystalline sp^2 structure.

Alternatively, there was a sustained decrease in the A_{D1}/A_G and A_{D1}/A_{D3} values and increase in the A_{D3}/A_G value for 1FeJXO15-800H, 3FeJXO15-800H, and 6FeJXO15-800H, whereas a gentle increase in the A_{D4}/A_G value was observed, as shown in Fig. 10. It could be inferred that the presence of $FeCl_3$ catalyst could change the reaction pathways between the carbon structure and activated gas; the small aromatic ring systems and active sites could no longer be consumed with activated gas preferentially; the big aromatic rings would begin to decompose into small aromatic rings,[47,48] and the $FeCl_3$ catalyst could hinder the formation of the crystalline sp^2 structure. In other words, the catalysts appeared to be preferentially accommodated on the carbons of aromatic nature, and more new cross-linking structures were formed from the broken fragments that resulted from the breakdown of aromatic structures by the catalytic capacity of $FeCl_3$ catalyst. Moreover, the presence of O-containing structures was conducive to the reorganization of aromatic fragments. However, catalysts might move gradually and agglomerate with each other on the char surface at high burn-offs; this would lead to the degradation of catalysis for 6FeJXO15-800H.

3.7. Pore structure development of typical chars during activation

To analyze the pore development of JX-800, 1FeJXO15-800H, 3FeJXO15-800H, and 6FeJXO15-800H at different burn-off values during activation, the N_2 adsorption isotherms, the

Table 5 Raman data of coal chars at different burn offs during activation

Samples	I_{D1}/I_G	I_{D3}/I_G	I_{D4}/I_G	I_{D1}/I_{D3}
JX-800	3.197	1.922	0.611	1.663
JX-800-15.4	3.754	1.845	0.503	2.034
JX-800-28.8	4.514	1.797	0.314	2.511
JX-800-58.2	2.64	1.545	0.107	1.708
1FeJXO15-800H	3.770	2.715	0.849	1.388
1FeJXO15-800H-14.6	3.515	3.001	0.853	1.171
1FeJXO15-800H-22.9	3.089	3.450	0.864	0.895
3FeJXO15-800H	3.877	2.820	0.885	1.375
3FeJXO15-800H-14.7	3.573	3.175	0.890	1.125
3FeJXO15-800H-22.5	3.053	3.725	0.973	0.819
6FeJXO15-800H	3.987	2.955	0.936	1.349
6FeJXO15-800H-14.5	3.712	3.145	0.940	1.180
6FeJXO15-800H-22.1	3.499	3.513	0.951	0.996

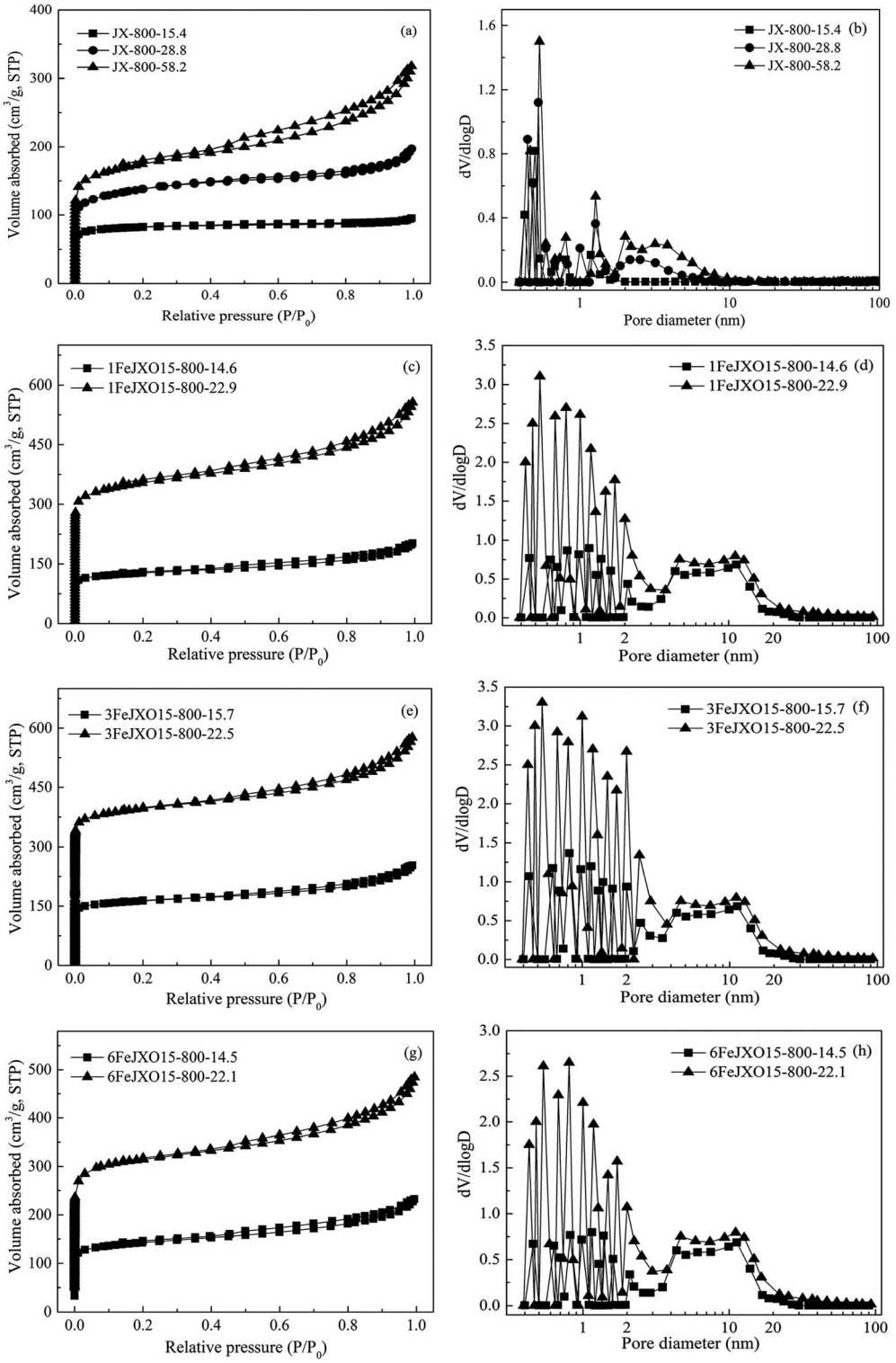

Fig. 7 N_2 adsorption isotherms and pore-size distributions of coal chars at different burn offs during activation.

pore-size distribution, and parameters of porous structure are shown in Fig. 7 and Table 6.

At first, based on Fig. 7, the isotherms of JX-800-15.4 could be classified as type I at low burn-offs, showing a narrow size distribution of less than 1 nm. With the gradual increase of burn-offs from 15.4% to 58.2%, all the N_2 isotherms exhibited the characteristics of type I at low pressures as well as that of type IV at high pressures, and the clear hysteresis loops were observed, showing the formation of the hierarchical structure. Then, the pore structure parameters of JX-800 at different burn

Table 6 Pore structure parameters of typical chars at different burn offs during activation

Samples	S_{BET} (m^2 g^{-1})	V_t (m^3 g^{-1})	V_{mic} (m^3 g^{-1})	Non-V_{mic} (%)	D_{ap} (nm)
JX-800-15.4	107.56	0.063	0.060	4.76	2.34
JX-800-28.8	305.45	0.154	0.127	17.53	2.02
JX-800-58.2	564.19	0.275	0.185	32.72	1.95
1FeJXO15-800H-14.6	348.45	0.192	0.140	27.08	2.20
1FeJXO15-800H-22.9	1045.43	0.344	0.285	17.15	1.32
3FeJXO15-800H-14.7	398.78	0.215	0.169	21.39	2.15
3FeJXO15-800H-22.5	1274.64	0.418	0.366	12.44	1.31
6FeJXO15-800H-14.5	326.55	0.184	0.130	29.34	2.25
6FeJXO15-800H-22.1	916.23	0.325	0.268	17.54	1.42

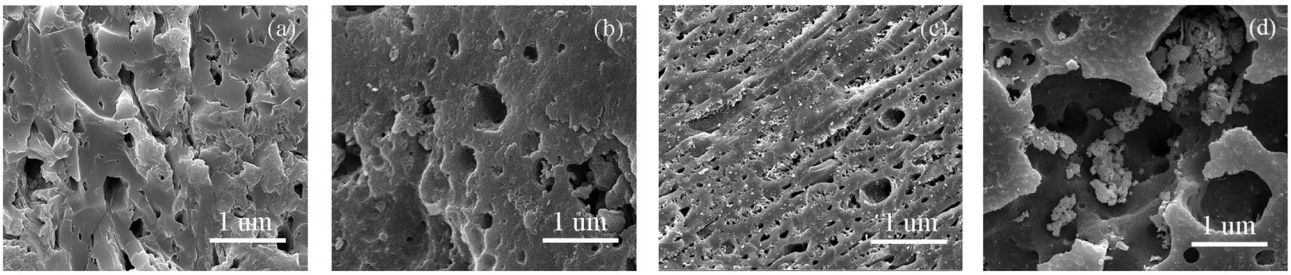

Fig. 8 SEM images of coal chars under final burn-off values (a) 1FeJXO15-800H-22.9 (b) 3FeJXO15-800H-22.5 (c) 6FeJXO15-800H-22.1 (d) JX-800-58.2.

offs during activation are included in Table 6. The S_{BET} value of 107.56 m^2 g^{-1}, V_{mic} value of 0.06 m^3 g^{-1}, and non-V_{mic} value of 4.76% for JX-800-15.4 were obtained, indicating the major development of micropores during the initial activation process. There was a sustained decrease in the S_{BET}, V_{mic}, and non-V_{mic} values with an increase in the burn-off from 15.4% to 58.2%. This increase could be associated with the enlargement of micropores into mesopores progressively and the formation of many new micropores during this stage of activation. However, compared to the development of new micropores, the rapid increase of non-V_{mic} value, namely, the increase and development of mesopore, was more obvious from about 28.8% burn-off. Finally, the S_{BET} value of 564.19 m^2 g^{-1} for JX-800-58.2 at relatively high burn offs was obtained, indicating a low S_{BET}/burn-off ratio value of 9.69 m^2 g^{-1}/%, and severe carbon losses on the particle surfaces could also be observed, as shown in Fig. 8(d). These results indicated that the pore formation of JX-800 with less initial pores followed the hierarchical development from the surface to the core during activation. Moreover, the ordered conversion of microstructure hindered the penetration of activated gas into the interior of char structure; this led to the occurrence of more reactions on the particle surfaces rather than in the interior to decrease the production of the pores.

Alternatively, the adsorption capacities of 1FeJXO15-800H, 3FeJXO15-800H, and 6FeJXO15-800H increased rapidly at low pressures, but had little changes at high pressures with an increase in the burn-off from 14.5% to 22.9%; this indicated the major development of micropores. The S_{BET} and V_{mic} values rapidly increased during the whole stage of activation, whereas the non-V_{mic} value decreased drastically with the increasing burn-off. These changes meant that the initial pores of 1FeJXO15-800H, 3FeJXO15-800H, and 6FeJXO15-800H acted as channels to help the diffusion of activated gas, and the oxygen-containing active sites could strengthen the etching of the carbon structure. Along with the gradual consumption of oxygen functional groups, the disordered conversion of carbon structure and more active sites in the presence of Fe-based compounds facilitated a sustained production of more micropores; this resulted in the rapid increase of the S_{BET}, V_t, and V_{mic} values. Although the catalysts might have moved and agglomerated on the particle surfaces for 6FeJXO15-800H with an increase of burn-off, no severe carbon losses occurred on the particle surface, as observed in Fig. 8(a)–(c). Importantly, the effects of oxygen functional groups and $FeCl_3$ catalyst could further facilitate the rapid development of micropores at a relatively low burn off. The S_{BET} values (1045.43, 1274.64, and 916.23 m^2 g^{-1}) of 1FeJXO15-800H, 3FeJXO15-800H, and 6FeJXO15-800H at the relatively low burn-off values of 22.9%, 22.5%, and 22.1% were obtained, indicating the high values S_{BET}/burn-off ratio of 45.65 m^2 g^{-1}/%, 56.65 m^2 g^{-1}/%, and 41.46 m^2 g^{-1}/%, respectively.

4 Conclusions

Physical activation of Jixi bituminous coal regulated by oxygen functional groups (created by air pre-oxidation at 200 °C for 15 h) and $FeCl_3$ (1 wt%, 3 wt%, and 6 wt%) has provided a good control of micro- and macro-structure of Jixi bituminous char throughout the preparation process to obtain the ideal AC

production with a high S_{BET} at low burn-off values. In the phase of pyrolysis, the existence of oxygen functional groups could improve the distributed formation of $FeCl_3$ catalyst in the interior of the particle, hindering the concentration and amalgamation of $FeCl_3$ catalyst at high temperatures and promoting the catalytic characteristics. The effects of oxygen functional groups and $FeCl_3$ catalyst could further promote the disordered conversion of microstructure and the number of active sites, but catalytic cracking characteristics of the $FeCl_3$ catalyst could play a more important role. In addition, $FeCl_3$ could efficaciously promote the development of micropores, and the evolution of oxygen functional groups mainly facilitated the production of mesopores and macropores. In the phase of activation, the reaction pathway of active sites and activated gas was changed by the presence of the $FeCl_3$ catalyst; this resulted in a consistent disordered conversion of the microstructure of 1FeJXO15-800H, 3FeJXO15-800H, and 6FeJXO15-800H as compared to the ordered conversion of JX-800. The effects of oxygen functional groups and $FeCl_3$ catalyst could promote the favorable diffusion of activated gas throughout more initial pores produced by oxygen functional groups, following non-hierarchical development. With an increase in activation time, the existence of $FeCl_3$ catalyst could facilitate the etching of the carbon structure; this resulted in a rapid and continuous development of the micropores rather than the severe carbon losses on the particle surface. Finally, the S_{BET} values (1045.43, 1274.64, and 916.23 $m^2\ g^{-1}$) of 1FeJXO15-800H-22.9, 3FeJXO15-800H-22.5, and 6FeJXO15-800H-22.1 were obtained, indicating the high S_{BET}/burn-off ratio values of 45.65 $m^2\ g^{-1}$/%, 56.65 $m^2\ g^{-1}$/%, and 41.46 $m^2\ g^{-1}$/%, respectively, as compared to the relatively low S_{BET} 564.19 $m^2\ g^{-1}$ of JX-800-58.2, indicating a low S_{BET}/burn-off ratio value of 9.69 $m^2\ g^{-1}$/%.

Conflicts of interest

There are no conflicts of interest to declare.

Acknowledgements

The authors greatly acknowledge the financial support received from the research project supported by the National Natural Science Foundation of China (51276052) and (51476047).

References

1 F. Sun, J. H. Gao, X. Liu, X. F. Tang and S. H. Wu, *Appl. Surf. Sci.*, 2015, **357**, 1895–1901.
2 S. Shu, J. X. Guo, X. L. Liu, X. J. Wang, H. Q. Yin and D. M. Luo, *Appl. Surf. Sci.*, 2016, **360**, 684–692.
3 B. Rubio and M. T. Izquicrdo, *Fuel*, 1998, **77**, 631–637.
4 A. A. Lizzio and J. A. Debarr, *Fuel*, 1996, **75**, 1515–1522.
5 H. Teng, J. A. Ho and Y. F. Hsu, *Carbon*, 1997, **35**, 275–283.
6 H. Teng, J. A. Ho, Y. F. Hsu and C. T. Hsieh, *Ind. Eng. Chem. Res.*, 1996, **35**, 4043–4049.
7 B. A. Akash and W. S. OBrien, *Int. J. Eng. Res.*, 1996, **20**, 913–922.
8 G. San Miguel, G. D. Fowler and C. J. Sollars, *Carbon*, 2003, **41**, 1009–1061.
9 Y. W. Zhu, J. H. Gao, Y. Li, F. Sun, J. M. Gao, S. H. Wu and Y. K. Qin, *J. Taiwan Inst. Chem. Eng.*, 2012, **43**, 112–119.
10 Y. W. Zhu, J. H. Gao, Y. Li, F. Sun and Y. K. Qin, *Korean J. Chem. Eng.*, 2011, **28**, 2344–2350.
11 X. X. Zhou, X. Qu, R. Zhang and J. C. Bi, *Fuel Process. Technol.*, 2015, **135**, 195–202.
12 P. L. Walker, *Carbon*, 1996, **34**, 1297–1299.
13 M. M. Maroto-Valer, J. M. Andrés and C. Snape, *Energy Fuels*, 1997, **11**, 4036–4042.
14 K. Kidena, K. Matsumoto, S. Murata and M. Nomura, *Energy Fuels*, 2004, **18**, 1709–1715.
15 X. J. Li, J. I. Hayashi and C. Z. Li, *Fuel*, 2006, **85**, 1509–1517.
16 G. de la Puente, G. Marbán, E. Fuente and J. J. Pis, *J. Anal. Appl. Pyrolysis*, 1998, **44**, 205–218.
17 F. Heras, N. Alonso, M. A. Gilarranz and J. J. Rodriguez, *Ind. Eng. Chem. Res.*, 2009, **48**, 4664–4670.
18 F. Heras, N. Alonso-Morales, D. Jiménez-Cordero, M. A. Gilarranz and J. J. Rodriguez, *Ind. Eng. Chem. Res.*, 2012, **51**, 2609–2614.
19 D. Jiménez-Cordero, F. Heras, N. Alonso-Morales, M. A. Gilarranz and J. J. Rodriguez, *Chem. Eng. J.*, 2013, **231**, 172–181.
20 D. Jiménez-Cordero, F. Heras, N. Alonso-Morales, M. A. Gilarranz and J. J. Rodriguez, *Fuel Process. Technol.*, 2014, **118**, 148–155.
21 D. Jiménez-Cordero, F. Heras, M. A. Gilarranz and E. Raymundo-Piñero, *Carbon*, 2014, **71**, 127–138.
22 D. D. Liu, J. H. Gao, Q. X. Cao, S. H. Wu and Y. K. Qin, *Energy Fuels*, 2017, **31**, 1406–1415.
23 Y. Q. Wu, J. J. Wang, S. Y. Wu, S. Huang and J. S. Gao, *Fuel Process. Technol.*, 2011, **92**, 523–530.
24 S. J. Yuh and E. E. Wolf, *Fuel*, 1983, **62**, 252–255.
25 D. W. McKee, *Fuel*, 1983, **62**, 170–175.
26 I. L. C. Freriks, H. M. H. VanWechem and J. C. M. Freriks, *Fuel*, 1981, **60**, 463–470.
27 D. D. Liu, J. H. Gao, S. H. Wu and Y. K. Qin, *RSC Adv.*, 2016, **6**, 87478–87485.
28 W. C. Xu and A. Tomita, *Fuel Process. Technol.*, 1989, **21**, 25–37.
29 N. A. Oztas and Y. Yürüm, *Fuel*, 2000, **79**, 1221–1227.
30 X. Z. Gong, Z. C. Guo and Z. Wang, *Energy Fuels*, 2009, **23**, 4547–4552.
31 G. A. Zickler, B. Smarsly, N. Gierlinger, H. Peterlik and O. Paris, *Carbon*, 2006, **44**, 3239–3246.
32 X. J. Li, H. Jun-ichiro and C. Z. Li, *Fuel*, 2006, **85**, 1700–1707.
33 K. B. Yang, J. H. Peng, H. Y. Xia, L. B. Zhang, C. Srinivasakannan and S. H. Guo, *J. Taiwan Inst. Chem. Eng.*, 2010, **41**, 367–372.
34 M. Belhachemi, R. V. R. A. Rios, F. Addoun, J. Silvestre-Albero, A. Sepúlveda-Escribano and F. Rodrìguez-Reinoso, *J. Anal. Appl. Pyrolysis*, 2009, **86**, 168–172.
35 R. Pietrzak, *Fuel*, 2009, **139**, 1871–1877.
36 N. Karatepe, Ì. Orbak, R. Yavuz and A. Özyuğuran, *Fuel*, 2008, **87**, 3207–3215.

37 H. Mori, K. Asami and Y. Ohtsuka, *Energy Fuels*, 1996, **10**, 1022–1027.
38 Y. Ohtsuka, T. Watanabe, K. Asami and H. Mori, *Energy Fuels*, 1998, **12**, 1356–1362.
39 Y. Ohtsuka, C. B. Xu, D. P. Kong and N. Tsubouchi, *Fuel*, 2004, **83**, 685–692.
40 W. Li and Y. M. Zhu, *Energy Fuels*, 2014, **28**, 3645–3654.
41 K. Murakami, H. Shirato, J. I. Ozaki and Y. Nishiyama, *Fuel Process. Technol.*, 1996, **46**, 183–194.
42 L. H. William and B. Michel, *Fuel*, 1983, **62**, 132–165.
43 T. Li, L. Zhang and D. Li, *Fuel*, 2014, **117**, 1190–1195.
44 C. D. Sheng, *Fuel*, 2007, **86**, 2316–2324.
45 A. Sasezky, H. Muckenhuber and H. Grothe, *Carbon*, 2005, **43**, 1731–1742.
46 H. L. Tay and C. Z. Li, *Fuel Process. Technol.*, 2010, **91**, 800–804.
47 H. L. Tay, S. Kajitani, S. Zhang and C. Z. Li, *Fuel*, 2013, **103**, 22–28.
48 X. Guo, L. T. Hui, S. Zhang and C. Z. Li, *Energy Fuels*, 2008, **22**, 4034–4038.